Revealing the Underlying Solvent Effect on Film Morphology in High-Efficiency Organic Solar Cells by Combined *Ex-situ* and *In-situ* Observations

Ruijie Ma[1,5], Xinyu Jiang[2,5], Jiehao Fu[1], Tao Zhu[1], Cenqi Yan[1], Kexin Wu[2], Peter Müller-Buschbaum[2,4]*, Gang Li[1,3]*

[1]Department of Electronic and Information Engineering, Research Institute for Smart Energy (RISE), Guangdong-Hong Kong-Macao (GHM) Joint Laboratory for Photonic-Thermal-Electrical Energy Materials and Devices, The Hong Kong Polytechnic University, Hung Hom, Kowloon, Hong Kong, 999077, China
Email: gang.w.li@polyu.edu.hk

[2]Lehrstuhl für Funktionelle Materialien, Physik Department, Technische Universität München, James-Franck-Str. 1, 85748 Garching, Germany
Email: muellerb@ph.tum.de

[3]The Hong Kong Polytechnic University Shenzhen Research Institute, Shenzhen, 518057, China

[4]Heinz Maier-Leibnitz Zentrum (MLZ), Technische Universität München Lichtenbergstr. 1, 85748 Garching, Germany

[5]Equal contribution

Abstract

The morphology features and the film formation processes in high-performance donor-acceptor binary photovoltaic blends cast from three representative solvents are carefully investigated and analyzed. The PM6:L8-BO system shows a very significant efficiency change when varying the solvent from chloroform (CF) to chlorobenzene (CB) and o-xylene (XY), whereas the PM6:eC9 system shows a limited influence of the used solvent. *Ex-situ* characterizations figure out that CB and XY cause a too-pronounced phase separation for PM6:L8-BO. In contrast, PM6:eC9 films display only slightly enlarged phase segregation in CB films and an even better mixing in XY-processed films. The *in-situ* observations further reveal that the PM6 aggregation-dominated stage during the film formation is longer for the eC9 system than that of L8-BO, effectively suppressing the separation of donor and acceptor. PM6 is found to be very miscible with the acceptors when processed from XY. The *ex-situ* analysis results correlate well with the device performance and are finely explained by the *in-situ* and miscibility study. Further, an excellent device efficiency of 19.10 % (verified 18.77%) is achieved by a ternary design for XY-enabled organic solar cells (OSCs) by PTQ10, while the corresponding blade coating devices present an excellent PCE of 18.25%. Thereby, this work produces a clear understanding of film morphology formation and realizes high-performance non-halogenated solvent-processed OSCs.

Key words: morphology, solvent, efficiency, organic solar cells, in-situ study

Introduction

Due to a successful boosting of the power conversion efficiency (PCE) to over 19% in single-junction and over 20% in tandem architectures, organic solar cells (OSCs) are expected to move forward in the global photovoltaic (PV) market.[1-11] Today, lab progress in OSCs heavily relies on material design and the research community continuously generates new donor and acceptor materials, to realize higher PCEs that can guarantee the competitiveness of OSCs against other PV technologies. From the

aspect of device engineering, the halogenated solvent chloroform (CF) is usually the priority for processing new materials due to its excellent solubility.[12-18] However, CF exhibits high toxicity and carcinogenicity, which seriously will challenge any large-scale use.[19-20] Moreover, the low boiling point (BP) characteristics of CF also challenge the solar cell fabrication process. Thus, using non-halogenated solvents with high BPs is highly appreciated for establishing a large-scale ambient fabrication of OSCs in the futures.

The most common processing solvents for state-of-the-art OSC systems, such as CF, chlorobenzene (CB), and xylene (XY) have different BPs, vapor pressures and solubilities. Thus, the film drying processes vary from one solvent to another, resulting in differently tuned morphology.[21-28] Therefore, understanding the observed PCE variations must be substantiated by an in-depth morphology analysis, enabled by advanced characterization methods including *ex-situ* and *in-situ* technologies.[29-37] Furthermore, a tight connection between morphological features and device performance needs to be established.[38-40]

Herein, we chose two representative high-PCE photovoltaic systems, namely PM6:eC9 & PM6:L8-BO,[41-42] processed from CF, CB and XY, respectively, to study the film morphology and device performance in a systematic manner. (Full name of the materials shown in the SI) PM6 is selected as donor material due to its good solubility and featured pre-aggregation in the precursor, while eC9 and L8-BO are two non-fullerene acceptors that showed record PCEs when paired with PM6 in the literature.[41-42] CF and CB are both halogen solvents, which offer similar solubilities, whereas their BP difference leads to different film formation process. For XY (non-halogenated), the BP is similar with that of CB. Consequently, the efficiencies of PM6:eC9 processed from CF, CB and XY are 17.79 %, 17.52 % and 18.16 %, respectively. The respective PCE values of PM6:L8-BO are 18.31 %, 15.79 % and 16.75 %. These results show that changing the solvent does not apparently affect the PV performances of the eC9 based system, but significantly alters the PCEs of the L8-BO based devices. The *ex-situ* morphology study reveals that both material systems cast from CF exhibit the

morphology characteristics of a well miscible phase distribution, as well as interpenetrating networks with long and thick nanofibers. The CB and XY processed films show an enhanced polymer aggregation and donor/acceptor phase separation, but eC9 based active layers display morphological features much closer to CF processed ones compared to the L8-BO based counterparts do. Although the film drying durations for different systems processed by the same solvents are identical, the aggregation behaviors of PM6 and the two NF acceptors are quite different when high BP solvents are used: The PM6 aggregation dominated time is shorter, and the acceptor aggregation dominated period is longer in the PM6:L8-BO system, compared to PM6:eC9. Thereby a less intermixing film morphology will be established. Further experimental results suggest that the miscibility of PM6:eC9 is better than that of PM6:L8-BO, which is beneficial for keeping a favorable intermixing morphology when longer evaporation times occur. In the view of the excellent PCE achieved in case of PM6:eC9 films processed from the non-halogenated solvent XY, the known ternary blend construction strategy of introducing PTQ10 is applied to achieve even higher PCEs.[43-44] In the case of 20 % PTQ10 substituting PM6 in the blend, a further improved PCE of 19.10 % is realized, one of the best PCEs of OSC devices processed from eco-friendly solvents reported so far (verified PCE 18.77% by an independent organization). Meanwhile, corresponding blade coating devices enabled by advanced methods of reversing and N_2 knife assisted solidification achieve decent efficiency of 18.25%, too. Thereby, on the one hand this study is meaningful in understanding the solvent effect in determining thin film morphologies and device efficiency, and on the other hand it is an encouraging attempt of combining *ex-situ* and *in-situ* studies to elucidate the morphology evolution.

Results and Discussion

The chemical structures of PM6, eC9 and L8-BO are shown in **Figure 1a** together with the processing solvents CF, CB and XY, which have BPs of 61.2 ℃, 132 ℃, 144 ℃, respectively. Accordingly, when using spin coating for the film deposition, CF processed solutions tend to evaporate quickly, while the CB and XY-based solutions

require a longer time to form the solid active layers. Kinetically, the prolonged film drying time will generate a different aggregation behavior of the donor and acceptor materials.

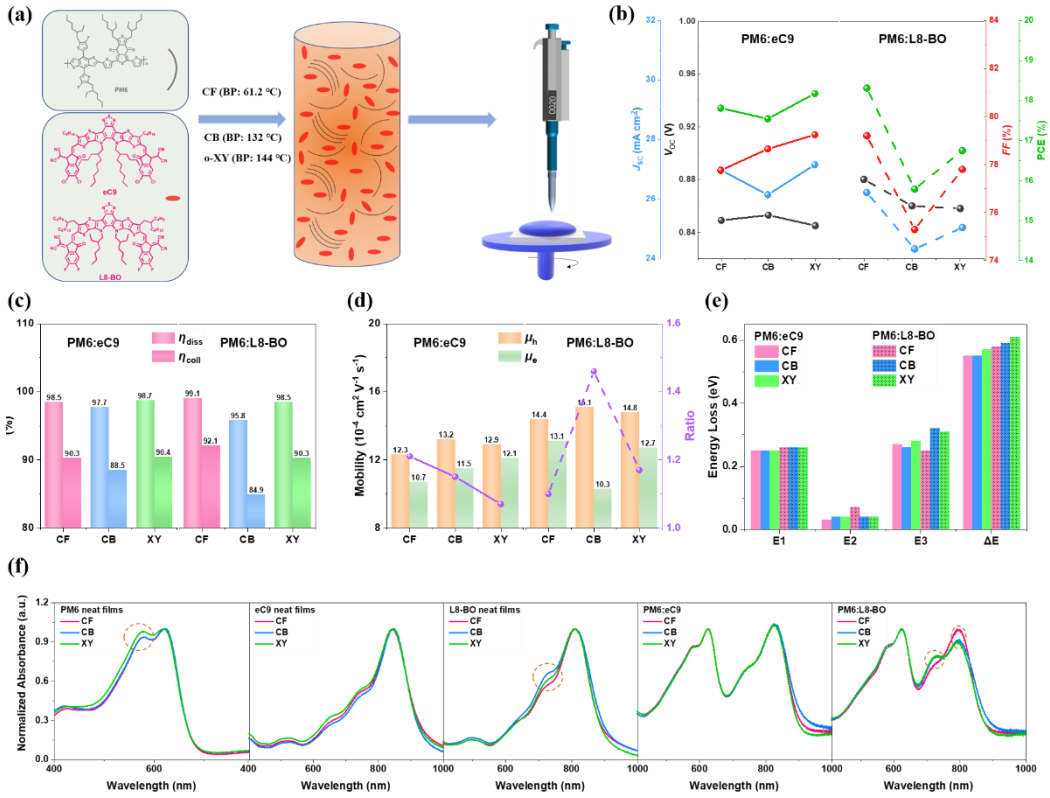

Figure 1. (a) Chemical structures of donor and acceptors, processing solvents, mixing solution state, and spin coating sketch. (b) V_{OC}, J_{SC}, *FF* and PCE average values of CF, CB and XY processed devices based on PM6:eC9 and PM6:L8-BO. (c) Calculated values of charge generation and collection rates for the investigated systems. (d) μ_h, μ_e values and their ratios of each system. (e) Energy loss summary. (f) Thin film UV-vis absorption spectra of PM6, eC9, L8-BO, and their blends.

We make a series of OSCs for CF, CB and XY processed PM6:eC9 and PM6:L8-BO systems based on the conventional device structure of ITO/ PEDOT:PSS-TA (tyramine doped)/ active layers/ PFN-Br-MA (melamine doped)/ Ag.[45-46] The optimal current density vs voltage (*J*-*V*) characteristics and the external quantum efficiency (EQE) spectra are shown in **Figure S1**. The numerical statistics from 20 independent devices for each type of active layer, are presented in **Figure S2-S3** and **Table S1**. A detailed comparison based on averaged open-circuit voltage (V_{OC}), short-circuit current density

(J_{SC}), fill factor (*FF*) and PCE values is summarize in **Figure 1b**. Accordingly, the PCE variation as function of the processing solvent is insignificant for PM6:eC9 blends compared with PM6:L8-BO ones. The PCE of CF processed PM6:eC9 OSCs is 17.79 %, which is consistent with previous reports.[41] In the case of CB, the PCE of PM6:eC9 is 17.52 %, with a higher V_{OC} and *FF*, but a lower J_{SC}. Notably, the best PCE is achieved for XY-processed devices, reaching values as high as 18.16 %, which is a state-of-the-art value for binary OSCs enabled by non-halogen solvents. Despite the lowest V_{OC}, XY-processed devices have outstanding J_{SC} and *FF* values. Moreover, the CF-processed devices based on PM6:L8-BO blends display an optimal PCE of 18.31 %, with the best V_{OC}, J_{SC} and *FF* values, in comparison with its CB- and XY-processed counterparts. The lowest efficiency values for PM6:L8-BO blends are found when using CB, where all three parameters V_{OC}, J_{SC} and *FF* are reduced. In the case of XY-processed OSCs, a distinguishable efficiency is reached due to higher J_{SC} and *FF* values. The results from these device studies match well with the integrated external quantum efficiency (EQE) spectra, which suggests that the errors are below 3%.

Next, we investigate the photocurrent density (J_{ph}) vs effective voltage (V_{eff}) relationships to evaluate the charge dissociation and collection of each studied system. The results are plotted in **Figure S4**, and the analysis method is elaborated in the **Supporting Information**, too. The derived η_{diss} and η_{coll} values are presented in **Figure 1c**. The CB-processed PM6:L8-BO films are significantly poorer herein. In addition, the bimolecular recombination rates are evaluated by fitting the slope of J_{SC} and illumination intensity in logarithmic presentation, as seen in **Figure S5**. The slopes of CF-, CB- and XY-processed PM6:eC9 and PM6:L8-BO based OSCs are 0.96, 0.98, 0.97 and 0.95, 0.97. 0.97, implying that the use of a high BP solvent can reduce the bimolecular recombination. Such behavior can be probably attributed to an inducing larger phase separation. Subsequently, the charge transport characteristics of all types of devices are evaluated by assessing the hole and electron mobilities (μ_h, μ_e) through the space charge limited current (SCLC) method. Hole-only and electron-only device *J-V* curves with logarithmic x-axis and y-axis are presented in **Figure S6** and **S7**,

together with derived slope curves, which ensures that the data are from the SCLC region.[1] The determined μ_h, μ_e and μ_h/μ_e values are shown in **Figure 1d**. The variation tendency of μ_h/μ_es is consistent with the corresponding *FFs*. Note that the highest μ_h value is achieved by CB-processed films and the lowest μ_e values by CF-processed films for both photoactive systems, implying that the aggregation behavior of PM6 is dominated by the processing solvent. Furthermore, since the V_{OC} variations of both systems are different, with a drastic drop in case of CB- and XY-processed PM6:L8-BO based devices, we carry out energy loss analysis upon all of them.[47] The Fourier transform photocurrent spectroscopy external quantum efficiency (FTPS-EQE) and electroluminescence (EL) spectra are given in **Figure S8**, and EQE_{EL} along applied current in **Figure S9**. The results of ΔE_1 (Shockley-Queisser loss), ΔE_2 (radiative loss below bandgap) and ΔE_3 (non-radiative loss) are calculated and summarized in **Figure 1e**. Apparently, the severe energy reduction in CB- and XY-processed PM6:L8-BO based solar cells is caused by significantly increased ΔE_3 of 0.32 eV and 0.31 eV, compared with the other 4 blends (0.25 eV ~ 0.28 eV). The detailed data can be also found in **Table S2**.

A variation of the processing solvent will definitely tune the morphology of the active layer to a different degree. However, in the present study, the device efficiency variation trends are complicated and non-monotonous with the order of rising BPs for two studied systems. Therefore, an in-depth study of the morphology is needed to establish a structure-property correlation. First, the ultra violet-visible (UV-vis) absorption spectra of neat PM6, eC9, L8-BO and their respective blend films are measured, to have a general comparison of the aggregation. As seen in **Figure 1f**, the CF- and CB-processed PM6 films show identical absorption profile, while the XY-processed film has a slightly higher 0-1 vibrational shoulder peak. Therefore, although the evaporation process is longer, the aggregation motif cannot be changed by using CB instead of CF, whereas a stronger *H*-aggregation is enabled by using XY. In case of the neat acceptor films, for the three studied solvents the eC9 films display no clear difference in the UV-vis spectra, while the L8-BO films exhibit a distinguishable shoulder peak height difference, which

satisfies CB > XY > CF. The PM6:eC9 blend films show three identical absorption spectra irrespective of the used solvent, indicating that the solvent does not affect thoroughly the general aggregation motif. In contrast, the PM6:L8-BO blend films processed from CB and XY have a significantly lower 0-0 peak and a higher 0-1 peak. Such observation suggests that the longer evaporation process has seriously changed the morphology from a favorable to an unfavorable one, when taking the device performance into account. This issue will be sophisticatedly analyzed in later part, via various characterizations.

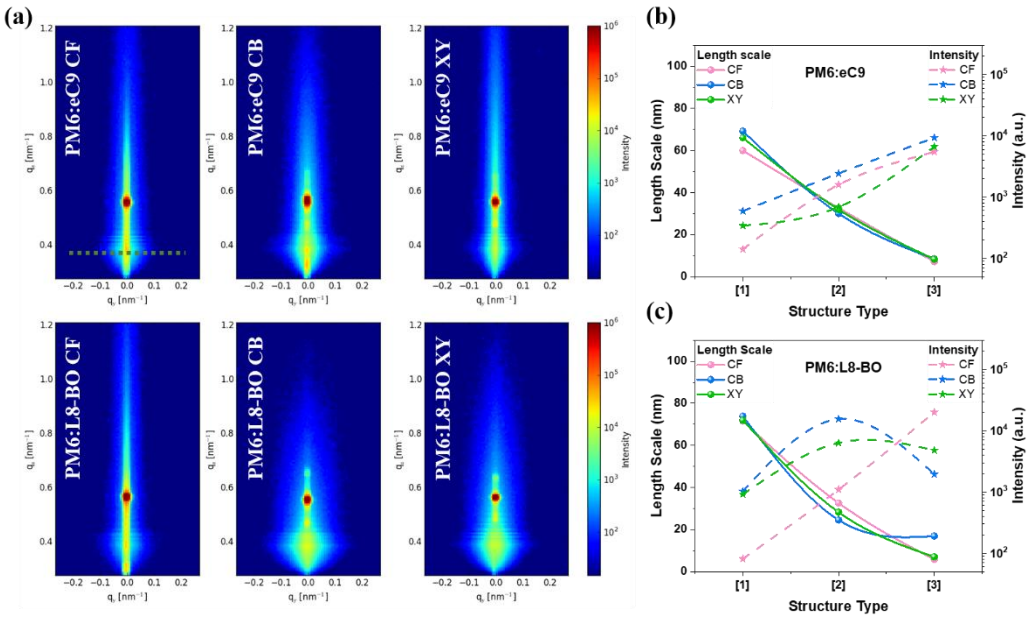

Figure 2. (a) 2D GISAXS data, the green dash line represents the critical angle of the active layer materials. Nano-structure domain radii and intensities for type [1] (large), [2] (medium), [3] (small) structures of (b) PM6:eC9 and (c) PM6:L8-BO systems.

The first concern of morphology analysis is the donor-acceptor phase separation, for which a quantitative illustration is enabled by grazing incidence small-angle X-ray scattering (GISAXS) experiments.[48-50] The 2D GISAXS data are presented in **Figure 2a**, and horizontal line cuts at the Yoneda region of the active layer are shown in **Figure S10**. To model the lateral structures of the active layer, cylindrical and spherical objects with different radii are used in the framework of the distorted wave Born approximation (DWBA) assuming the effective interface approximation (EIA).[51] Three domain

structures of different length scales and intensities are extracted from the fits and shown in **Figure 2b-2c,** respectively. The large domain radii (over 60 nm) represent aggregates inside the active layer, with the apparent lowest intensity distribution across all radii in case of the CF-processed active layer. Thus, GISAXS reveals that the CF solvent favors donor and acceptor mixing. Domains on the order of ten nanometers exhibit structural dimensions, which are suitable in size for splitting excitons into separate charge carriers.[52-53] Therefore the small radii (under 10 nm) play an important role, when judging the active layer quality. For PM6:eC9 blends, the CB cast film has the highest proportion not only in the small radii but also in the large and medium radii scales, suggesting a strong phase segregation, thus slightly undermining the charge carrier transport. The reduction of medium radii in XY-processed films, as well as the intensity, implies that XY provokes donor-acceptor intermixing more than CF for PM6:eC9. On the other hand, CF-processed PM6:L8-BO films also have a dominant small-scale phase with 5.8 nm size, and minor ratio of medium sized domains. These four blend films are of generally similar type concerning their phase distribution, which refers to an efficiency-favorable one. However, a drastic change happens in CB-processed PM6:L8-BO films: The medium structure radii intensity becomes 15 times stronger than that of the small structure radii, which suggests that the film morphology alters into a strong phase separation instead of a highly intermixing. A similar tendency is observed in the XY-processed PM6:L8-BO films, but the intensity difference between medium and small structures is not that severe (about 9 times). Such finding means that the XY-processed films exhibit a morphology with milder phase separation than the undesired CB-processed PM6:L8-BO.

The above results are also substantiated by the direct observations in the transmission electron microscopy (TEM) images, as shown in **Figure S11**. The CF-processed films of both, PM6:eC9 and PM6:L8-BO, possess a well-mixed donor-acceptor phase, which is beneficial for charge generation. Moreover, they show distinguishable long and narrow fibrils (pure phase), and well mixed bright and dark phases with small length scales, which is consistent with GISAXS calculation results. In the case of PM6:L8-BO

films cast from CB and XY, a significant phase self-aggregation is observed (CB > XY), so the GISAXS results of them are directly supported. As for CB and XY processed eC9 based blend films, the general feature of phase separation observed from images is very similar - consistent with GISAXS data, too. It is somehow understandable that longer drying times endow a more significant phase separation for donor and acceptor. However, in PM6:eC9 blend films, the situation is completely different. Starting from the solvent CF, well mixed and interpenetrating multi-length scale features are enabled. Only CB-processed films have a slightly enhanced phase segregation that corresponds to its J_{SC} loss in the respective devices. The ideal morphology re-occurs in XY-processed films, which is consistent with the increased J_{SC} and *FF* values, but requires further explanation. Note there might be some ideas of TEM image comparison is not significant enough, which is in essence reasonable for preaggregation property of PM6, but this part of study can be a solid side-evidence for the already precise quantitative analysis of GISAXS.

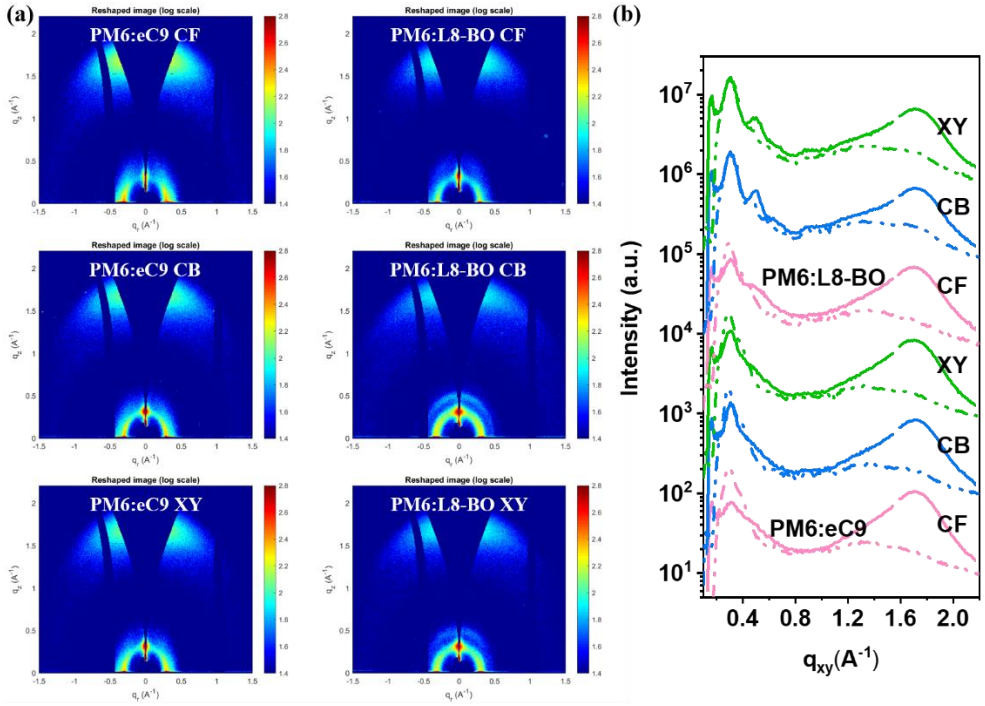

Figure 3. (a) 2D GIWAXS data and (b) corresponding cake cuts in the IP (dash) and OOP (solid) direction.

The film crystallinity, as a result of material crystallization behavior, is further

studied using the grazing incidence wide-angle X-ray scattering (GIWAXS) technique.[54-56] Enclosed in **Figure 3a -3b** are 2D GIWAXS data and the related cake cuts in the in plane (IP) and out-of-plane (OOP) directions. The related fit parameters are summarized in **Table S3 -S5**. The (100) peak representing the PM6 lamellar diffraction exhibits a 20.9 Å d-spacing for all PM6:eC9 films irrespective of the solvent and for CF-processed PM6:L8-BO films. A reduced value of 20.2 Å is found for CB- and XY-processed PM6:L8-BO films. The coherence length (CL) values of them are 57.7, 79.7, 58.3, 71.6, 52.9 and 51.4 Å, orderly. In the (010) peak that reflects π-π stacking property, the d-spacing values are 3.72 Å, 3.72 Å, 3.74 Å for eC9 and 3.74 Å, 3.72 Å, 3.70 Å for L8-BO systems when processed from CF, CB, XY, and the corresponding CL values of these peaks are17.0, 18.2, 17.0, 18.9, 18.5 and 18.6 Å, respectively. These results demonstrate the independent crystallization of donor and acceptor materials in a lamellar packing and π-π stacking scenario when using different solvents studied here. On the contrary, the co-crystallization varies significantly from solvent to solvent for the investigated systems. Compared with the PM6:eC9 films, the PM6:L8-BO-CF films show a decelerated intensity reduction from ~ 0.4 $Å^{-1}$ to ~ 0.6 $Å^{-1}$ irrespective of the processing solvent, since L8-BO tends to form its own nano-fibrils and forms a bi-continuity network.[1] In addition, CB-processed PM6:L8-BO films display an additional peak located at ~ 0.49 $Å^{-1}$ along the OOP direction, corresponding to a CL of 91.2 Å (~ 7 consecutive crystallites). It represents a large amount of L8-BO being separated from the PM6 phase, since the original co-crystallization is broken. Besides, the XY-processed L8-BO films also demonstrate a similar peak (~ 0.47 $Å^{-1}$) with a weaker intensity, which has a very small CL of 7.1 Å. This finding indicates the incomplete independent crystallization in the lamellar region or in other words, a recovered co-crystallization and intermixing to some extent. To get deeper insights into the orientation distribution of the crystallites, we perform tube cuts from the 2D GIWAXS data in a q range from 0.2 to 0.4 $Å^{-1}$, which is along the (100) peak. The percentage of edge-on, face-on, and isotropic oriented crystallites calculated by integrating the areas of the corresponding features in the pole figures (corrected I(χ) ×

sin(χ) vs χ plots) is shown in **Figure S12-S13** and **Table S6**. For PM6:eC9 thin films, the face-on orientation of the crystallites covers 81.7 %, 63.3 % and 59.9 % and the isotropic orientation is 18.0 %, 35.2 %, 39.4 % when processed from CF, CB and XY, respectively. Thus, we find a face-on-dominated orientation in the PM6:eC9 thin films, which provides favorable conditions for the charge carrier pathway in OSCs. Similarly, a face-on-dominated orientation is also confirmed in the PM6:L8-BO films processed from CF representing 63.1 % of the crystallites and the isotropic orientation is 36.5 %. However, an increased isotropic orientation of 58.8 % and 54.3 % dominates the crystallites in the CB- and XY-processed PM6:L8-BO thin films, respectively. Such dominating isotropic orientation hinders the charge carrier transport in these blend thin films. However, though with a higher percentage of isotropic orientation in the XY processed PM6:eC9 samples, it shows better donor and acceptor intermixing than with CF (confirmed by GISAXS), and it shows the best device performance.

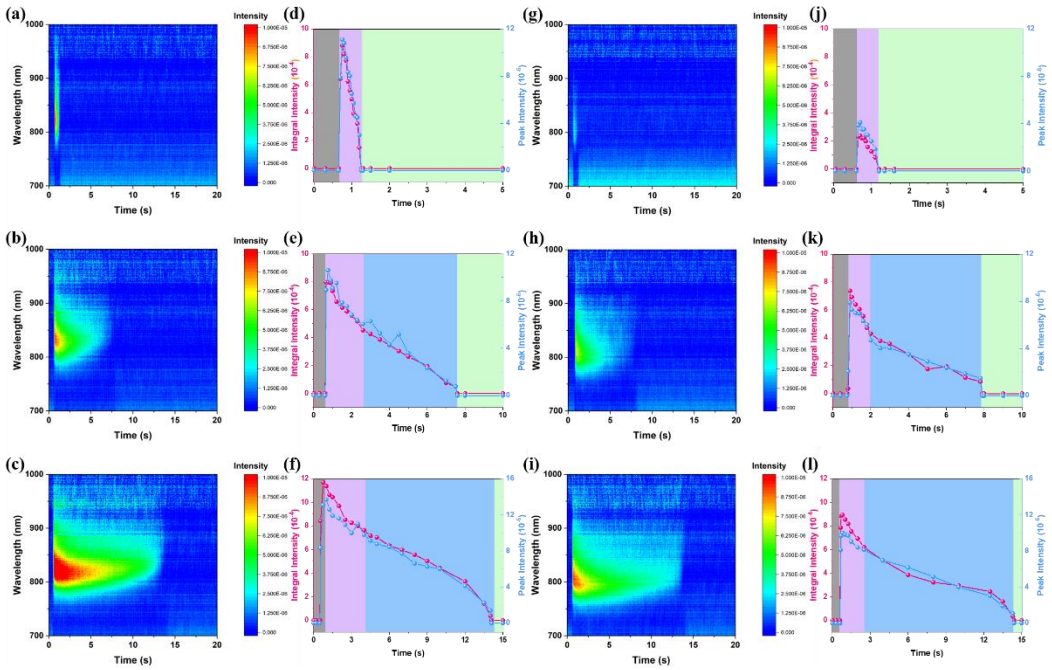

Figure 4. Contour maps of time resolved PL spectra for the PM6:eC9 system cast from (a) CF, (b) CB and (c) XY; corresponding calculated parameters in the case of (d) CF, (e) CB and (f) XY. Contour maps of time resolved PL spectra for PM6:L8-BO system cast from (g) CF, (h) CB and (i) XY; corresponding calculated parameters in the case of (j) CF, (k) CB and (l) XY. Gray region: before spin coating; purple region: polymer aggregation dominated stage; blue region: small molecule aggregation domination; green region: main solvent completely removed.

To elucidate the similarities and dissimilarities of the morphology variation tendencies as function of the processing solvent, we study the film formation process. With time dependent-photoluminescence (PL) we are signifying the specific stage of film drying, material aggregation, and the film formation processes.[57-59] In **Figure 4** the contour maps of the PL intensities are shown for systems of the present study, with their main peak position, intensity and total area values. The whole drying process is divided into three stages, which are marked as purple, blue and green regions. In addition, the gray region refers to the substrate spinning before the start of the solution coating. Both investigated systems show a very quick and linear decrease of the PL integrated peak areas in case of the CF-processing, which means that the donor and the acceptor aggregate and crystallize together. Such behavior is beneficial for maintaining the initial intermixing morphology. In case of the high BP solvent drying processes, the solvent evaporation clearly shows two stages, based on the change of the peak intensity and integrated area curve slopes. The purple region includes a fast drop of the integral intensity signals due to an enhancement and distance reduction of the chromophores. This trend results from the polymer aggregation (major contribution) and from the small molecule precipitation (minor contribution). Within the blue region, the integral PL peak areas decrease with a slower speed, being indicative of a completion of the polymer aggregation and of the formation of a network structure. Therefore, this stage is dominated by the small molecule aggregation and crystallization, since its solubility is better and its aggregation tendency is weaker than that of the polymer. We note that in the present study the PM6 dominated aggregation stage is obviously shorter in PM6:L8-BO system compared with PM6:eC9 systems, although the total durations of the CB- and XY-processed film drying are almost identical for both. Thus, L8-BO separates from PM6 in the liquid phase quicker than eC9 does. Accordingly, the CB- and XY-processed PM6:L8-BO films display a larger phase segregation morphology, which is not found in the corresponding PM6:eC9 films. Furthermore, one interesting phenomenon in the blue region of XY related film is noticed. In the blue region for NFA

dominated drying, a faster signal drop at tail is observed for XY systems, while rather monotonic intensity reduction occurs in CF and CB ones. Guided by previous literature, we assign this phenomenon to the role of DIO additive.[60] When the ratio of DIO comes to some level, the acceptor will be induced as aggregates even in the process of liquid-to-solid transition, thus slightly increased emission. Their result explains the slower signal decrease in XY than in CB at the most part of blue region. It is supported by that DIO's molar ratio in XY main solvent is higher than in CB. At the end of blue stage, all chromophores quickly get quenched due to the complete drying.

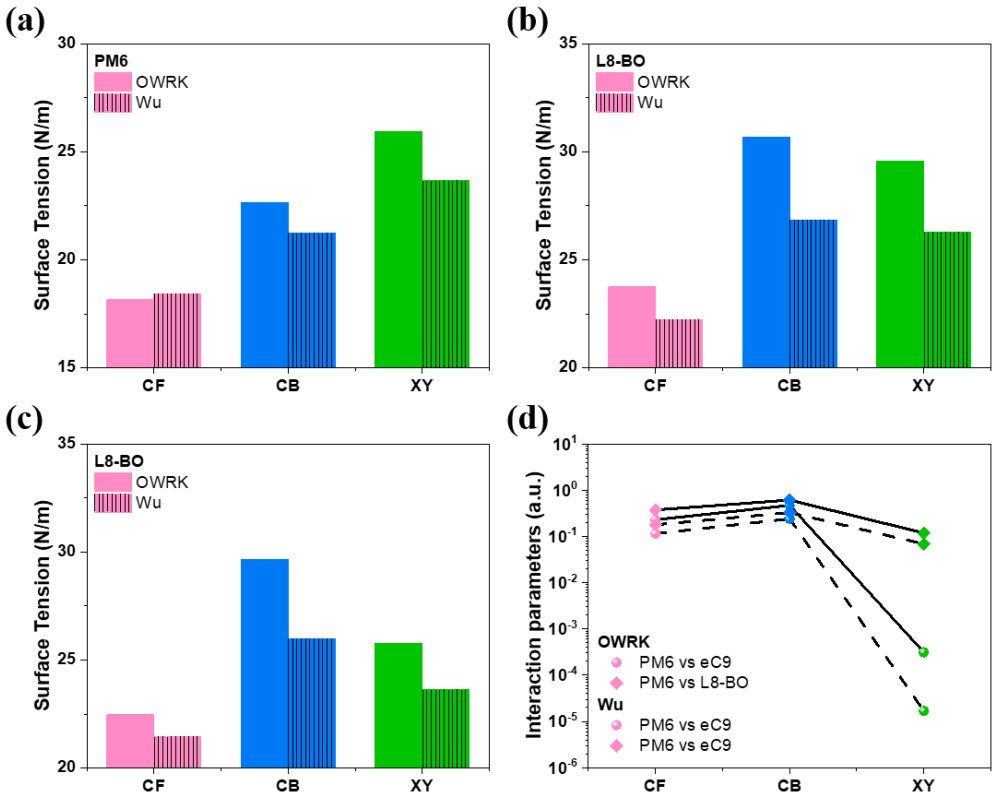

Figure 5. Surface tensions of PM6, eC9 and L8-BO neat films from different solvents calculated from two algorithms (Wu and OWRK models), and deduced interaction (miscibility) parameters.

After figuring out the underlying reason for the enlarged phase separation in PM6:L8-BO films when using BP solvent processing, our next target is to understand the morphology recovery in the XY-films. Thus, a miscibility assessment is carried out based on contact angle experiments.[61-62] The neat films of PM6, eC9 and L8-BO

processed from the three solvents studied here are exposed to water and ethylene glycol (EG) droplets. The formed droplets are displayed in **Figure S14**. The determined surface tensions are presented in **Figure 5a** to **5c**, based on two different algorithms. **Figure 5d** plots the related interaction (miscibility) parameters accordingly. It is found that the miscibility parameters are at a similar level for PM6 vs eC9 and PM6 vs L8-BO in the CF and CB processed films, meaning that the enlarged phase separation is mainly due to the film drying kinetics. XY-processed PM6 and L8-BO films also indicate a similar miscibility (slightly lower). Thereby, the recovery degree of the XY-processed film morphologies is limited. Moreover, we can see that PM6 and eC9 are highly miscible with each other as well, so the highly mixed donor-acceptor distribution in their blend films is well explained.

In addition, these findings also demonstrate why CF is often a preferred choice in device optimization when new materials are introduced. Based on its low BP and fast evaporation kinetics, photoactive materials regardless of being polymers or small molecules are going to intermix with each other well during the initial blending in the liquid phase, and a subsequent aggregation or crystallization can be finely tuned by post treatments such as annealing and the use of volatile additives. Moreover, the material selection principle for gaining high-efficiency eco-friendly solvent processed OSCs can be preliminarily established. It is that the material-material-solvent interaction in the solution state shall deliver a well miscible morphology in the initially cast films. As for further optimization, if crystallinity and phase separation should be enhanced, there would be enough space for post treatments (solvent additive, thermal annealing, solvent vapor fumigation etc.) to pursue the desired film morphology.

Another interesting point worths discussion is to correlate the relationship between morphology features and V_{OC}. A simple claim is over-separated phases without enough nanofibrils such as CB and XY processed PM6:L8-BO active layers suffers great loss in both V_{OC} and J_{SC}, but one noticeable issue is that CB type PM6:eC9 has larger phase separation while achieving higher V_{OC} than its CF and XY counterparts. For this point, we suppose the slightly enlarged phase separation only causes loss in J_{SC}, but nothing

negative to V_{OC} and *FF*, which is also widely observed in the whole field as a result of properly increased phase purity.

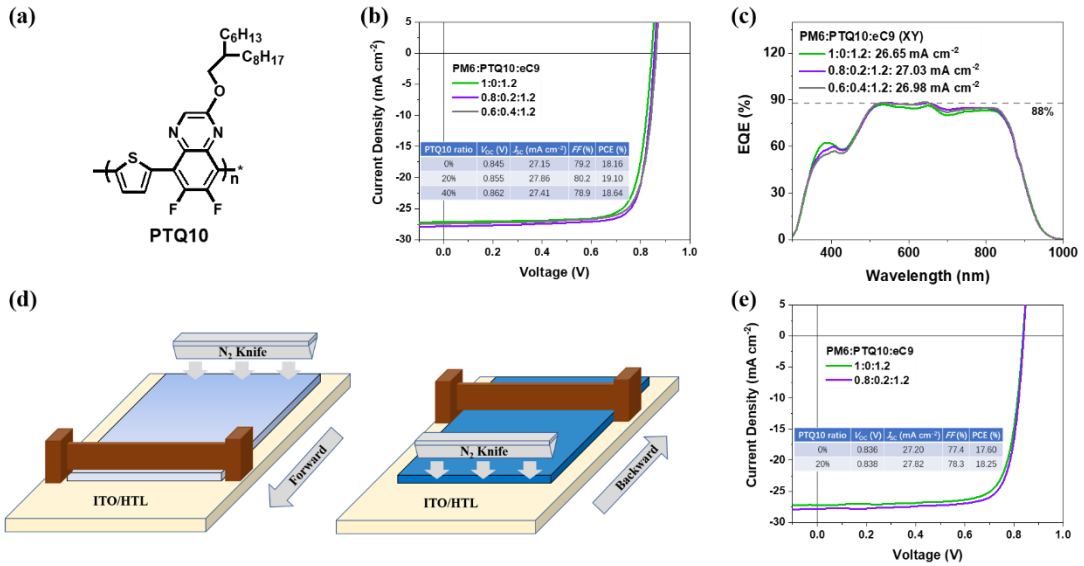

Figure 6. (a) Chemical structure of PTQ10. (b) *J-V* characteristics. (c) EQE spectra. (d) Schematic diagram of blade coating and (e) *J-V* characteristics.

Importantly, binary solar cells based on PM6:eC9 can produce a PCE over 18 %, when processed from XY, which is an encouraging result for eco-friendly solvent processed OSCs. A further efficiency enhancement is pursued by ternary strategy - PM6:PTQ10:eC9. An increase PCE is expected from the synergy of PM6 and PTQ10, in combination with the fact that PTQ10 can be well dissolved by XY as well. The chemical structure of PTQ10 is given in **Figure 6a**. The related photovoltaic parameters of the studied ternary devices with varied compositions are shown in **Figure 6b** as *J-V* characteristics with the characteristic parameters shown in the inserted table. The best efficiency of 19.10 % is gained by selecting 20 % of PTQ10, which demonstrates an appealing advance in the progress of OSCs.[65-72] For completeness, the EQE spectra of these devices are also provided in **Figure 6c**. To put our finding into a literature perspective, **Figure S15** delivers a brief comparison of our result against other reported non-halogenated solvent processed OSC devices. Details are given in **Table S7**. For a further confirmation, an independent third-party verification upon this result is carried out and presented in **Figure S16**.

Furthermore, the importance of non-halogenated solvent's utilization is for printing compatible film coating, so the open-air blade coating devices based on PM6:eC9 and optimal PM6:PTQ10:eC9 systems were fabricated with N_2-knife assisted coating.[73-77] The schematic diagram is drawn in **Figure 6d**, while the photovoltaic parameters and *J-V* curves of the devices are shown in **Figure 6e** (EQE spectra in **Figure S17**). The high efficiencies are also obtained as high as 17.60% and 18.25% for binary and optimal ternary blend systems, respectively. Such results are also among the highest values by blade coating to date.

Conclusion

In summary, motivated by the popular solvent choice (CF) for device fabrication in recent OSC works, and considering large-scale fabrication solvent requirements (moderately high BP), we studied a series of devices based on two high-efficiency systems (PM6:eC9 and PM6:L8-BO) by selecting three representative solvents: CF, CB and XY. Comprehensive *ex-situ* and *in-situ* investigations along with device data allow us to recognize the favorable morphology with intermixing phase distribution and nano-fibril formed network. Moreover, the ideal film formation type is identified, i.e.: having a fast solvent evaporation, which leaves no time for an undesired to strong phase separation. Furthermore, the successful PCE improvement in XY-processed PM6:eC9 based OSCs and the miscibility study suggest that achieving high-efficiency in similar type systems would also require that the donor and acceptor materials are highly miscible. A mature ternary matrix is built to boost the efficiency of non-halogenated solvent enabled OSCs (both spin and blade coating), which results in very high values. Thereby, this work demonstrates comprehensively combined *ex-situ* and *in-situ* investigations, resolves several morphological issues, and provides in depth understanding and suggestions for a further development of OSC's material and device engineering.

Note

The authors declare no conflict of interest.

Acknowledgement

G. L. acknowledges the support from Research Grants Council of Hong Kong (Project Nos 15221320, C5037-18G), RGC Senior Research Fellowship Scheme (SRFS2223-5S01), National Natural Science Foundation of China (51961165102), Shenzhen Science and Technology Innovation Commission (JCYJ20200109105003940), the Hong Kong Polytechnic University Internal Research Funds: Sir Sze-yuen Chung Endowed Professorship Fund (8-8480), RISE (Q-CDA5), G-SAC5, 1-YW4C and Guangdong-Hong Kong-Macao Joint Laboratory for Photonic-Thermal-Electrical Energy Materials and Devices (GDSTC No. 2019B121205001). P.M.B appreciates the support from the Deutsche Forschungsgemeinschaft (DFG, German Research Foundation) Grant No. Mu1487/22, the International Research Training Group 2022 Alberta/Technical University of Munich International Graduate School for Environmentally Responsible Functional Hybrid Materials (ATUMS) and under Germany's Excellence Strategy – EXC 2089/1 – 390776260 (e conversion), TUM. solar in the context of the Bavarian Collaborative Research Project Solar Technologies Go Hybrid (SolTech) and the Center for NanoScience (CeNS). R.M. thanks the support by PolyU distinguished Postdoctoral Fellowship. X.J. acknowledges the financial support from the Chinese Scholarship Council (CSC). Dr. Wei Gao of City University of Hong Kong is appreciated for the help with device performance verification.

Author Contribution

Ruijie Ma: Conceptualization, Investigation, Formal Analysis, Writing – Original Draft, Methodology, Validation

Xinyu Jiang: Investigation, Formal Analysis, Methodology, Writing – Original Draft

Jiehao Fu: Validation

Tao Zhu: Investigation

Cenqi Yan: Investigation

Kexin Wu: Investigation

Peter Müller-Buschbaum: Resources, Supervision, Writing – Review & Editing, Funding Acquisition

Gang Li: Resources, Supervision, Writing – Review & Editing, Funding Acquisition

Reference

1. L. Zhu, M. Zhang, J. Xu, C. Li, J. Yan, G. Zhou, W. Zhong, T. Hao, J. Song, X. Xue, Z. Zhou, R. Zeng, H. Zhu, C.-C. Chen, R. C. I. MacKenzie, Y. Zou, J. Nelson, Y. Zhang, Y. Sun and F. Liu, *Nat. Mater.*, 2022, **21**, 656-663.

2. Y. Cui, Y. Xu, H. Yao, P. Bi, L. Hong, J. Zhang, Y. Zu, T. Zhang, J. Qin, J. Ren, Z. Chen, C. He, X. Hao, Z. Wei and J. Hou, *Adv. Mater.*, 2021, **33**, 2102420.

3. L. Zhan, S. Li, Y. Li, R. Sun, J. Min, Y. Chen, J. Fang, C.-Q. Ma, G. Zhou, H. Zhu, L. Zuo, H. Qiu, S. Yin and H. Chen, *Adv. Energy Mater.*, 2022, **n/a**, 2201076.

4. W. Gao, F. Qi, Z. Peng, F. R. Lin, K. Jiang, C. Zhong, W. Kaminsky, Z. Guan, C.-S. Lee, T. J. Marks, H. Ade and A. K. Y. Jen, *Adv. Mater.*, 2022, **34**, 2202089.

5. R. Ma, C. Yan, J. Yu, T. Liu, H. Liu, Y. Li, J. Chen, Z. Luo, B. Tang, X. Lu, G. Li and H. Yan, *ACS Energy Lett.*, 2022, **7**, 2547-2556.

6. Y. Wei, Z. Chen, G. Lu, N. Yu, C. Li, J. Gao, X. Gu, X. Hao, G. Lu, Z. Tang, J. Zhang, Z. Wei, X. Zhang and H. Huang, *Adv. Mater.*, 2022, **34**, 2204718.

7. K. Chong, X. Xu, H. Meng, J. Xue, L. Yu, W. Ma and Q. Peng, *Adv. Mater.*, 2022, **34**, 2109516.

8. R. Sun, Y. Wu, X. Yang, Y. Gao, Z. Chen, K. Li, J. Qiao, T. Wang, J. Guo, C. Liu, X. Hao, H. Zhu and J. Min, *Adv. Mater.*, 2022, **34**, 2110147.

9. G. Liu, R. Xia, Q. Huang, K. Zhang, Z. Hu, T. Jia, X. Liu, H. L. Yip and F. Huang, *Adv. Funct. Mater.*, 2021, **31**, 2103283.

10. Z. Zheng, J. Wang, P. Bi, J. Ren, Y. Wang, Y. Yang, X. Liu, S. Zhang and J. Hou, *Joule*, 2022, **6**, 171-184.

11. Y. Huang, L. Meng, H. Liang, M. Li, H. Chen, C. Jiang, K. Zhang, F. Huang, Z. Yao, C. Li, X. Wan and Y. Chen, *J. Mater. Chem. A*, 2022, **10**, 11238-11245.

12. Y. Shi, Y. Chang, K. Lu, Z. Chen, J. Zhang, Y. Yan, D. Qiu, Y. Liu, M. A. Adil, W. Ma, X. Hao, L. Zhu and Z. Wei, *Nat. Commun.*, 2022, **13**, 3256.

13. C. Zhu, L. Meng, J. Zhang, S. Qin, W. Lai, B. Qiu, J. Yuan, Y. Wan, W. Huang and Y. Li, *Adv. Mater.*, 2021, **33**, 2100474.

14. Z. Luo, R. Ma, J. Yu, H. Liu, T. Liu, F. Ni, J. Hu, Y. Zou, A. Zeng, C.-J. Su, U. S. Jeng, X. Lu, F. Gao, C. Yang and H. Yan, *National Science Review*, 2022, **9**, nwac076.

15. Z. Luo, Y. Gao, H. Lai, Y. Li, Z. Wu, Z. Chen, R. Sun, J. Ren, C. e. Zhang, F. He, H. Woo, J. Min and C. Yang, *Energy Environ. Sci.*, 2022, DOI: 10.1039/D2EE01848A.

16. L. Zhu, M. Zhang, G. Zhou, T. Hao, J. Xu, J. Wang, C. Qiu, N. Prine, J. Ali, W. Feng, X. Gu, Z. Ma, Z. Tang, H. Zhu, L. Ying, Y. Zhang and F. Liu, *Adv. Energy Mater.*, 2020, **10**, 1904234.

17. T. Xu, J. Lv, K. Yang, Y. He, Q. Yang, H. Chen, Q. Chen, Z. Liao, Z. Kan, T. Duan, K. Sun, J. Ouyang and S. Lu, *Energy Environ. Sci.*, 2021, **14**, 5366-5376.

18. S. Li, L. Zhan, N. Yao, X. Xia, Z. Chen, W. Yang, C. He, L. Zuo, M. Shi and H. Zhu, *Nat. Commun.*, 2021, **12**, 1-11.

19. T. A. Jorgenson, E. F. Meierhenry, C. J. Rushbrook, R. J. Bull and M. Robinson, *Fundam. Appl. Toxicol.*, 1985, **5**, 760-769.
20. W. Guan, D. Yuan, J. Wu, X. Zhou, H. Zhao, F. Guo, L. Zhang, K. Zhou, W. Ma and W. Cai, *J. Semi.*, 2021, **42**, 030502-030502-030504.
21. L. Ye, Y. Xiong, Q. Zhang, S. Li, C. Wang, Z. Jiang, J. Hou, W. You and H. Ade, *Adv. Mater.*, 2018, **30**, 1705485.
22. S. Dong, T. Jia, K. Zhang, J. Jing and F. Huang, *Joule*, 2020, **4**, 2004-2016.
23. L. Ye, S. Zhang, W. Ma, B. Fan, X. Guo, Y. Huang, H. Ade and J. Hou, *Adv. Mater.*, 2012, **24**, 6335-6341.
24. R. Ma, T. Yang, Y. Xiao, T. Liu, G. Zhang, Z. Luo, G. Li, X. Lu, H. Yan and B. Tang, *ENERGY & ENVIRONMENTAL MATERIALS*, 2022, **5**, 977-985.
25. Z. Li, L. Ying, P. Zhu, W. Zhong, N. Li, F. Liu, F. Huang and Y. Cao, *Energy Environ. Sci.*, 2019, **12**, 157-163.
26. C. Sprau, F. Buss, M. Wagner, D. Landerer, M. Koppitz, A. Schulz, D. Bahro, W. Schabel, P. Scharfer and A. Colsmann, *Energy Environ. Sci.*, 2015, **8**, 2744-2752.
27. D. Wang, H. Liu, Y. Li, G. Zhou, L. Zhan, H. Zhu, X. Lu, H. Chen and C.-Z. Li, *Joule*, 2021, **5**, 945-957.
28. L. Zhu, W. Zhong, C. Qiu, B. Lyu, Z. Zhou, M. Zhang, J. Song, J. Xu, J. Wang, J. Ali, W. Feng, Z. Shi, X. Gu, L. Ying, Y. Zhang and F. Liu, *Adv. Mater.*, 2019, **31**, 1902899.
29. L. Ye, H. Hu, M. Ghasemi, T. Wang, B. A. Collins, J.-H. Kim, K. Jiang, J. H. Carpenter, H. Li, Z. Li, T. McAfee, J. Zhao, X. Chen, J. L. Y. Lai, T. Ma, J.-L. Bredas, H. Yan and H. Ade, *Nat. Mater.*, 2018, **17**, 253-260.
30. K. Zhou, K. Xian, Q. Qi, M. Gao, Z. Peng, J. Liu, Y. Liu, S. Li, Y. Zhang, Y. Geng and L. Ye, *Adv. Funct. Mater.*, 2022, **32**, 2201781.
31. J. Xin, X. Meng, X. Xu, Q. Zhu, H. B. Naveed and W. Ma, *Matter*, 2019, **1**, 1316-1330.
32. K. Gao, W. Deng, L. Xiao, Q. Hu, Y. Kan, X. Chen, C. Wang, F. Huang, J. Peng, H. Wu, X. Peng, Y. Cao, T. P. Russell and F. Liu, *Nano Energy*, 2016, **30**, 639-648.
33. Z. Peng, L. Ye and H. Ade, *Materials Horizons*, 2022, **9**, 577-606.
34. S. Engmann, F. A. Bokel, H. W. Ro, D. M. DeLongchamp and L. J. Richter, *Adv. Energy Mater.*, 2016, **6**, 1502011.
35. F. Liu, S. Ferdous, E. Schaible, A. Hexemer, M. Church, X. Ding, C. Wang and T. P. Russell, *Adv. Mater.*, 2015, **27**, 886-891.
36. L. J. Richter, D. M. DeLongchamp and A. Amassian, *Chem. Rev.*, 2017, **117**, 6332-6366.
37. W. Zhong, M. Zhang, G. Freychet, G. M. Su, L. Ying, F. Huang, Y. Cao, Y. Zhang, C. Wang and F. Liu, *Adv. Mater.*, 2022, **34**, 2107316.
38. H. Chen, R. Zhang, X. Chen, G. Zeng, L. Kobera, S. Abbrent, B. Zhang, W. Chen, G. Xu, J. Oh, S.-H. Kang, S. Chen, C. Yang, J. Brus, J. Hou, F. Gao, Y. Li and Y. Li, *Nat. Energy*, 2021, **6**, 1045-1053.
39. R. Ma, K. Zhou, Y. Sun, T. Liu, Y. Kan, Y. Xiao, T. A. Dela Peña, Y. Li, X. Zou, Z. Xing, Z. Luo, K. S. Wong, X. Lu, L. Ye, H. Yan and K. Gao, *Matter*, 2022, **5**, 725-734.
40. T. Hao, W. Zhong, S. Leng, R. Zeng, M. Zhang, L. Zhu, Y. Yang, J. Song, J. Xu, G. Zhou, Y. Zou, Y. Zhang and F. Liu, *Sci. China Chem.*, 2022, **65**, 1634-1641.
41. Y. Cui, H. Yao, J. Zhang, K. Xian, T. Zhang, L. Hong, Y. Wang, Y. Xu, K. Ma, C. An, C. He, Z. Wei, F. Gao and J. Hou, *Adv. Mater.*, 2020, **32**, 1908205.

42. C. Li, J. Zhou, J. Song, J. Xu, H. Zhang, X. Zhang, J. Guo, L. Zhu, D. Wei, G. Han, J. Min, Y. Zhang, Z. Xie, Y. Yi, H. Yan, F. Gao, F. Liu and Y. Sun, *Nat. Energy*, 2021, **6**, 605-613.
43. L. Arunagiri, Z. Peng, X. Zou, H. Yu, G. Zhang, Z. Wang, J. Y. Lin Lai, J. Zhang, Y. Zheng, C. Cui, F. Huang, Y. Zou, K. S. Wong, P. C. Y. Chow, H. Ade and H. Yan, *Joule*, 2020, **4**, 1790-1805.
44. W. Zhang, C. Sun, I. Angunawela, L. Meng, S. Qin, L. Zhou, S. Li, H. Zhuo, G. Yang, Z.-G. Zhang, H. Ade and Y. Li, *Adv. Mater.*, 2022, **34**, 2108749.
45. R. Ma, M. Zeng, Y. Li, T. Liu, Z. Luo, Y. Xu, P. Li, N. Zheng, J. Li, Y. Li, R. Chen, J. Hou, F. Huang and H. Yan, *Adv. Energy Mater.*, 2021, **11**, 2100492.
46. X. Xiong, X. Xue, M. Zhang, T. Hao, Z. Han, Y. Sun, Y. Zhang, F. Liu, S. Pei and L. Zhu, *ACS Energy Lett.*, 2021, **6**, 3582-3589.
47. Y. Wang, D. Qian, Y. Cui, H. Zhang, J. Hou, K. Vandewal, T. Kirchartz and F. Gao, *Adv. Energy Mater.*, 2018, **8**, 1801352.
48. X. Jiang, P. Chotard, K. Luo, F. Eckmann, S. Tu, M. A. Reus, S. Yin, J. Reitenbach, C. L. Weindl, M. Schwartzkopf, S. V. Roth and P. Müller-Buschbaum, *Adv. Energy Mater.*, 2022, **12**, 2103977.
49. Z. Wang, K. Gao, Y. Kan, M. Zhang, C. Qiu, L. Zhu, Z. Zhao, X. Peng, W. Feng, Z. Qian, X. Gu, A. K. Y. Jen, B. Z. Tang, Y. Cao, Y. Zhang and F. Liu, *Nat. Commun.*, 2021, **12**, 332.
50. D. Yang, F. C. Löhrer, V. Körstgens, A. Schreiber, B. Cao, S. Bernstorff and P. Müller-Buschbaum, *Adv.Sci.* 2020, **7**, 2001117.
51. X. Jiang, H. Kim, P. S. Deimel, W. Chen, W. Cao, D. Yang, S. Yin, R. Schaffrinna, F. Allegretti, J. V. Barth, M. Schwager, H. Tang, K. Wang, M. Schwartzkopf, S. V. Roth and P. Müller-Buschbaum, *J. Mater. Chem. A*, 2020, **8**, 23628-23636.
52. S. Athanasopoulos, S. Tscheuschner, H. Bässler and A. Köhler, *The Journal of Physical Chemistry Letters*, 2017, **8**, 2093-2098.
53. M. T. Sajjad, A. Ruseckas and I. D. W. Samuel, *Matter*, 2020, **3**, 341-354.
54. J. Rivnay, S. C. B. Mannsfeld, C. E. Miller, A. Salleo and M. F. Toney, *Chem. Rev.*, 2012, **112**, 5488-5519.
55. H. Zhao, H. B. Naveed, B. Lin, X. Zhou, J. Yuan, K. Zhou, H. Wu, R. Guo, M. A. Scheel, A. Chumakov, S. V. Roth, Z. Tang, P. Müller-Buschbaum and W. Ma, *Adv. Mater.*, 2020, **32**, 2002302.
56. J. Fang, Z. Wang, J. Zhang, Y. Zhang, D. Deng, Z. Wang, K. Lu, W. Ma and Z. Wei, *Advanced Science*, 2015, **2**, 1500250.
57. H. Zhao, B. Lin, J. Xue, H. B. Naveed, C. Zhao, X. Zhou, K. Zhou, H. Wu, Y. Cai, D. Yun, Z. Tang and W. Ma, *Adv. Mater.*, 2022, **34**, 2105114.
58. Q. Zhu, J. Xue, G. Lu, B. Lin, H. B. Naveed, Z. Bi, G. Lu and W. Ma, *Nano Energy*, 2022, **97**, 107194.
59. Y. Liu, A. Yangui, R. Zhang, A. Kiligaridis, E. Moons, F. Gao, O. Inganäs, I. G. Scheblykin and F. Zhang, *Small Methods*, 2021, **5**, 2100585.
60. J. Xin, J. Feng, B. Lin, H. B. Naveed, J. Xue, N. Zheng and W. Ma, *Small*, 2022, **18**, 2200608.
61. R. Ma, T. Liu, Z. Luo, K. Gao, K. Chen, G. Zhang, W. Gao, Y. Xiao, T.-K. Lau, Q. Fan, Y. Chen, L.-K. Ma, H. Sun, G. Cai, T. Yang, X. Lu, E. Wang, C. Yang, A. K. Y. Jen and H. Yan, *ACS Energy Lett.*, 2020, **5**, 2711-2720.
62. T. Xu, J. Lv, K. Yang, Y. He, Q. Yang, H. Chen, Q. Chen, Z. Liao, Z. Kan, T. Duan, K. Sun, J. Ouyang and S. Lu, *Energy Environ. Sci.*, 2021, **14**, 5366-5376.
63. D. K. Owens and R. C. Wendt, *J. Appl. Polym. Sci.*, 1969, **13**, 1741-1747.

64. S. Wu, *Journal of Polymer Science Part C: Polymer Symposia*, 1971, **34**, 19-30.
65. Y. Xu, Y. Cui, H. Yao, T. Zhang, J. Zhang, L. Ma, J. Wang, Z. Wei and J. Hou, *Adv. Mater.*, 2021, **33**, 2101090.
66. D. Wang, G. Zhou, Y. Li, K. Yan, L. Zhan, H. Zhu, X. Lu, H. Chen and C.-Z. Li, *Adv. Funct. Mater.*, 2022, **32**, 2107827.
67. H. Lu, H. Wang, G. Ran, S. Li, J. Zhang, Y. Liu, W. Zhang, X. Xu and Z. Bo, *Adv. Funct. Mater.*, 2022, **32**, 2203193.
68. X. Song, P. Sun, D. Sun, Y. Xu, Y. Liu and W. Zhu, *Nano Energy*, 2022, **91**, 106678.
69. R. Sun, T. Wang, Y. Wu, M. Zhang, Y. Ma, Z. Xiao, G. Lu, L. Ding, Q. Zheng, C. J. Brabec, Y. Li and J. Min, *Adv. Funct. Mater.*, 2021, **31**, 2106846.
70. B. Fan, F. Lin, J. Oh, H. Fu, W. Gao, Q. Fan, Z. Zhu, W. J. Li, N. Li, L. Ying, F. Huang, C. Yang and A. K. Y. Jen, *Adv. Energy Mater.*, 2021, **11**, 2101768.
71. J. Wang, Y. Cui, Y. Xu, K. Xian, P. Bi, Z. Chen, K. Zhou, L. Ma, T. Zhang, Y. Yang, Y. Zu, H. Yao, X. Hao, L. Ye and J. Hou, *Adv. Mater.*, 2022, **34**, 2205009.
72. L. Zhan, S. Yin, Y. Li, S. Li, T. Chen, R. Sun, J. Min, G. Zhou, H. Zhu, Y. Chen, J. Fang, C.-Q. Ma, X. Xia, X. Lu, H. Qiu, W. Fu and H. Chen, *Adv. Mater.*, 2022, **n/a**, 2206269.
73. J. Zhang, L. Zhang, X. Wang, Z. Xie, L. Hu, H. Mao, G. Xu, L. Tan and Y. Chen, *Adv. Energy Mater.*, 2022, **12**, 2200165.
74. B. Zhang, F. Yang, S. Chen, H. Chen, G. Zeng, Y. Shen, Y. Li and Y. Li, *Adv. Funct, Mater.*, 2022, **32**, 2202011.
75. Y. Zhang, K. Liu, J. Huang, X. Xia, J. Cao, G. Zhao, P. W. K. Fong, Y. Zhu, F. Yan, Y. Yang, X. Lu and G. Li, *Nat. Commun.*, 2021, **12**, 4815.
76. P. W.-K. Fong, H. Hu, Z. Ren, K. Liu, L. Cui, T. Bi, Q. Liang, Z. Wu, J. Hao and G. Li, *Adv. Sci.*, 2021, **8**, 2003359.
77. Q. Bai, Q. Liang, H. Li, H. Sun, X. Guo and L. Niu, *Aggregate*, 2022, **n/a**, e281.